

Modeling pulse-cleaning plasma mirrors from dielectric response to saturation: A particle-in-cell approach

Cite as: Phys. Plasmas **26**, 103103 (2019); <https://doi.org/10.1063/1.5109683>

Submitted: 10 May 2019 • Accepted: 24 September 2019 • Published Online: 11 October 2019

 Ginevra E. Cochran,  Patrick L. Poole and  Douglass W. Schumacher



View Online



Export Citation



CrossMark

ARTICLES YOU MAY BE INTERESTED IN

[Fourier computed tomographic imaging of two dimensional fluorescent objects](#)

APL Photonics **4**, 106102 (2019); <https://doi.org/10.1063/1.5100525>

[Effect of spectral filtering on pulse duration in dissipative soliton resonance \(DSR\) regime of modelocked fiber laser](#)

Review of Scientific Instruments **90**, 106102 (2019); <https://doi.org/10.1063/1.5108771>

[Dual-color near-field imaging by means of thin-film plasmonic waveguide with precise beam control of multiple wavelengths](#)

Review of Scientific Instruments **90**, 103701 (2019); <https://doi.org/10.1063/1.5099505>

Physics of Plasmas

Papers from 62nd Annual Meeting of the
APS Division of Plasma Physics

Read now!



Modeling pulse-cleaning plasma mirrors from dielectric response to saturation: A particle-in-cell approach

Cite as: Phys. Plasmas **26**, 103103 (2019); doi: 10.1063/1.5109683

Submitted: 10 May 2019 · Accepted: 24 September 2019 ·

Published Online: 11 October 2019



View Online



Export Citation



CrossMark

Ginevra E. Cochran,^{1,a)} Patrick L. Poole,¹ and Douglass W. Schumacher²

AFFILIATIONS

¹Lawrence Livermore National Laboratory, 7000 East Ave, Livermore, California 94550, USA

²The Ohio State University, 191 West Woodruff Ave, Columbus, Ohio 43210, USA

^{a)}Electronic mail: cochran18@llnl.gov

ABSTRACT

Pulse-cleaning plasma mirrors are widely employed to improve ultraintense laser contrast, but much of the literature concerning their effect on the reflected pulse is empirical. A simulation study of pulse-cleaning plasma mirrors using the particle-in-cell code large scale plasma is presented. The importance of capturing initial ionization from neutral atoms, collisional effects, and simulation dimensionality is considered. Excellent agreement with experimental data is obtained when a multiphoton ionization model is employed. Furthermore, a series of 2D simulations is shown to accurately replicate both the reflected light intensity and mode obtained from full 3D simulations at significantly reduced computation cost.

<https://doi.org/10.1063/1.5109683>

I. INTRODUCTION

Ultraintense laser experiments require significant contrast enhancements as intensity increases for applications such as ion acceleration^{1–3} and attosecond pulse generation.⁴ Limiting temporal prepulse peak intensities to under 10^{-10} times that of the main pulse avoids excessive target expansion and ensures high fidelity laser matter interaction for current laser systems.^{5,6} In addition to modifications to laser architecture, laser contrast can be improved by the use of a pulse-cleaning plasma mirror.^{7,8} A transparent dielectric is placed at a position with respect to a focusing beam such that any prepulses are below the material's ionization threshold and transmit through, while the main pulse ionizes the surface and reflects from the resulting plasma. The ratio of high field reflectance to low field reflectance gives a measure of the improvement in contrast, and antireflection coatings on the front surface are commonly used to minimize reflections of the prepulse to well below a percent. The main pulse is reflected by the plasma with integrated reflectivities typically in the range of 70%–90% although this depends on parameters such as laser pulse duration, intensity, polarization, and angle of incidence.^{9,10}

However, a pulse-cleaning plasma mirror's direct effect on the laser pulse—reflected temporal profile and spatial mode—can be difficult to measure since it necessarily occurs at high intensity. In the study of metallic plasma mirrors for high harmonic generation, this is often investigated using particle-in-cell (PIC) simulations.^{11–13} While

some particle-in-cell simulations have focused on the incident laser's interaction with a preexisting plasma,^{14,15} only a few have included the ionization stage transition of the medium (from optically transparent to reflective),¹⁶ and none have examined plasma mirror behavior as a function of intensity. In a recent publication demonstrating liquid crystal films as renewable plasma mirrors,¹⁷ a particle-in-cell framework was benchmarked against experimental data for examining these effects. This work details the implementation of the simulation architecture that allows plasma mirror initiation to be considered—while simulation comparisons to the experimental work¹⁷ are highlighted as an example, the behavior of parameter selections detailed here will apply generally to any modeled dielectric material. Furthermore, the presented approach of using several two-dimensional simulations at different intensities to reconstruct the true three-dimensional result is demonstrated to be accurate and can also be applied to other materials. Plasma mirrors are key components for many high-field experiments, and they will become more important as higher pulse energies or intensities are used in future experiments. Accordingly, the development of a computational model can benefit these experiments.

PIC simulations are presented in Secs. II–VII which capture a pulse-cleaning liquid crystal plasma mirror as it is ionized, transitioning from a transparent dielectric to a plasma. Peak laser intensities between 2×10^{12} W/cm² and 9×10^{17} W/cm² are simulated, which span over five orders of magnitude from the ionization threshold of

the liquid crystal plasma mirror to past the optimum intensity observed for high-field reflectance. A brief overview of simulation parameters is given in Sec. II. Choosing an intensity-appropriate ionization model will be addressed in Sec. III and the effects of particle collisions at low-temperature in Sec. IV. Low field reflectance and corrections for simulation dimensionality are explained in Secs. V and VI, respectively. Finally, results using the full simulation methodology are discussed in Sec. VII.

II. SIMULATION PARAMETERS

These simulations were performed in 2D3V using the PIC code large scale plasma (LSP).¹⁸ An s-polarized laser ($\lambda = 800$ nm, beam waist = $1.2 \mu\text{m}$) is incident at 16° from target normal. The peak laser intensity was varied from 2×10^{12} to 9×10^{17} W/cm² to examine the plasma mirror behavior from the observed threshold intensity to well above the intensity corresponding to peak reflectance as seen in the experiment (the spot size is held fixed). The pulse was modeled as a Gaussian with a full-width at half maximum (FWHM) duration equal to 60 fs, and a total duration of 190 fs, corresponding to 4 orders of magnitude change in intensity over the pulse duration. The plasma mirror was modeled as a 270 nm thick slab of initially neutral hydrogen and carbon ($\rho_H = 5.35 \times 10^{22}/\text{cm}^3$, $\rho_C = 4.33 \times 10^{22}/\text{cm}^3$) with an initial temperature of 1 eV. The cell sizes were 2.5×3 nm, with 10 particles per species per cell. The simulations were explicit with absorbing boundary conditions and a Courant ratio of 0.75.

III. IONIZATION MODEL

In order to properly model the desired behavior of prepulse transmission, a pulse-cleaning plasma mirror must begin as a transparent dielectric; as a result, these simulations take the uncommon initial condition of neutral atoms. The experimental setup¹⁷ used the liquid crystal 4-octyl-4'-cyanobiphenyl (8CB) to form freestanding films.^{19,20} 8CB's molecular formula is $\text{C}_{21}\text{H}_{25}\text{N}$, and it has a density of ~ 1 g/cc. Since the ionization potentials of this molecule are not well known, 8CB here is treated as initially neutral hydrogen and carbon atoms with the appropriate densities based on the molecular formula.

The ionization mechanism by which a pulse-cleaning plasma mirror transitions from transparent dielectric to reflecting plasma and at what time this happens with respect to the rising edge of the pulse are critical for correctly modeling not only the reflected energy typically measured but also more elusive features such as pulse shortening.

Two limiting cases for possible photoionization mechanisms are multiphoton ionization (MPI)²¹ and tunneling ionization.²² In MPI, the ionization potential is overcome by several photons imparting their energy to the electron, allowing it to escape into the continuum for sufficient laser intensity. The lowest order MPI ionization rate can be described as

$$\Gamma_{N_{MPI}} = \sigma_{N_{MPI}} I_L^{N_{MPI}}, \quad (1)$$

where $\Gamma_{N_{MPI}}$ is the ionization rate of an electron with ionization potential I_p and photons of energy $h\nu$, which requires $N_{MPI} = I_p/(h\nu)$ photons (with N_{MPI} rounded up to the next integer). I_L here is the incident laser intensity, and $\sigma_{N_{MPI}}$ is the multiphoton ionization coupling coefficient.

Tunneling ionization takes place when the electric field of the laser deforms the atom's potential well, allowing an electron to tunnel through the depressed potential with some finite probability.

For hydrogen-like ions, the rate of tunneling ionization can be expressed as

$$\Gamma_{tunnel} \propto \frac{I_p^{5/2}}{I_L^{1/2}} e^{-2/3(I_p)^{3/2}/I_L^{1/2}}. \quad (2)$$

More advanced formulations such as the Ammosov-Delone-Krainov (ADK) model²³ take into account more complex ions.

In the limit where the height of the barrier drops below the ionization potential, the probability of ionization approaches 1—this is known as barrier suppression ionization (BSI).²⁴ The appearance intensity at which BSI takes place can be estimated as follows:

$$I_{app} = \frac{c\pi^2 \epsilon_0^3}{2Z^2 e^6} I_p^4, \quad (3)$$

where Z is the ion charge state after ionization, I_p is the ionization potential, c is the speed of light, ϵ_0 the vacuum permittivity, and e is the fundamental charge. 8CB is mostly hydrogen and carbon with appearance intensities of 1.4×10^{14} W/cm² and 6.4×10^{13} W/cm², respectively.

The Keldysh parameter²² provides a figure-of-merit for which ionization mechanism dominates and can be written as $\gamma = \sqrt{\frac{I_p}{2\Phi}}$, where $\Phi = e^2 I_L / 2m_e \omega_L^2 c \epsilon_0$ is the ponderomotive potential, m_e is the electron mass, and ω_L is the laser frequency. Typically it is required that $\gamma \approx 0.5$ or lower for tunneling rates to apply²⁵—alternately, the laser intensity at a given wavelength λ_L required to drive a given ionization potential in the tunneling regime can be written as $I_L \lambda_L^2$ ($\text{W}\mu\text{m}^2/\text{cm}^2$) = $2.15 \times 10^{13} \text{ cm}^2/(\text{W}\mu\text{m}^2 \text{ eV}) \times I_p$ (eV).

The mechanism by which a liquid crystal plasma mirror is ionized can thus be gauged by calculating the Keldysh parameters for the ionization potentials of its constituent hydrogens and carbons at intensities between the experimentally observed ionization threshold and these atoms' appearance intensities—i.e., $\sim 2 \times 10^{12}$ to $\sim 1 \times 10^{14}$ W/cm². Table I lists the Keldysh parameters at 5×10^{12} and 5×10^{13} W/cm² for C^{1+} , C^{2+} , H^+ , and 800 nm laser light. For all these charge states, $\gamma \geq 1.2$, suggesting a liquid crystal plasma mirror composed of these constituents will operate in the MPI regime. The ionization potentials of molecular 8CB are not well known; however, the first ionization level of benzene, C_6H_6^+ , which is present in 8CB, has been measured. Table I shows that it has a comparable Keldysh parameter at these intensities, suggesting that 8CB itself would also fall in the MPI regime. In fact, this will generally be the case for any dielectric-based plasma mirror. Typically intensities up to or above 10^{16} W/cm² will be present during

TABLE I. Relevant ionic/molecular charge states for 8CB. Ionization potentials^{26,27} are given in electronvolt, as well as number of photons required for MPI with 800 nm light and the Keldysh parameter γ for these charge states at 5×10^{12} and 5×10^{13} W/cm².

Species	I_p (eV)	N_{MPI}	γ (5×10^{12} W/cm ²)	γ (5×10^{13} W/cm ²)
C^{1+}	11.26	8	4.4	1.4
C^{2+}	24.38	16	6.4	2.0
H^+	13.60	9	4.8	1.5
C_6H_6^+	9.24	6	3.9	1.2

the operation of a plasma mirror, but ionization of hydrogen and carbon will have saturated well before these intensities are reached such that significant tunneling may never occur. Thus, the ionization profile required to correctly model this behavior is complex, with the central laser spot producing overdense plasma with multiple ionized species present while the wings generate an underdense plasma with only the first stage of ionization contributing.

Tunneling models such as ADK will greatly understate the ionization rates in the MPI regime, but use of MPI models in PIC is uncommon for ultraintense laser simulations—many simulations model metals or pulses with such high peak intensities that MPI-relevant intensities are not captured in the pulse due to computational constraints. For many materials, ionization potentials and ionization cross sections have been determined, either experimentally or through theory. However, there is no established MPI model for 8CB. More generally, it is not well established how a cold solid-density target becomes an ionized plasma under ultraintense, ultrafast laser excitation. In most PIC treatments, for example, the target is simply initialized as a plasma, but that is not acceptable here. However, given an initially sharp interface and ultrafast excitation, a kinetic approach is still a reasonable choice. Accordingly, an MPI model²¹ was added to LSP, where the single-particle probability of ionization in a time step is $P = (CE)^{2N_{MPI}}$ with an adjustable coefficient C , where E is the laser electric field and N_{MPI} is the minimum number of photons required for photoionization of the given species. The MPI coefficient of $C = 1 \times 10^{-9}$ cm/kV was chosen by matching the experimental reflectance at a single data point, $\sim 2 \times 10^{12}$, since this should be most sensitive to the ionization coefficient. This value was then used for simulations at all other intensities, spanning several orders of magnitude.

This is a heuristic approach designed to capture the transition to a plasma using only a single fitting coefficient. At low intensities and especially for a given stage of ionization, the coupling coefficient is approximately constant,²⁸ and the critical density is quickly reached. Plasma mirror reflectance is dominated by attainment of critical density and the saturated response at higher intensities. At high intensities, however, the intensity dependence is dominated by geometrical factors as the region where the intensity is saturated grows,²⁸ and this is captured by our model. Finally, Eq. (1) is based on intensity, not instantaneous electric field, and so the formulation implemented here in LSP will not have the same time dependence within a laser cycle. Despite this, the correct intensity dependence is achieved since laser intensity scales with photon density, which is the relevant physics at play.

IV. COLLISIONS AT LOW TEMPERATURES

PIC simulations typically do not represent physics within a Debye sphere such as particle collisions. This is due to finite cell size or, equivalently, the particle shape, and so when the problem calls for it, these effects must be added back in to the basic PIC cycle. These simulations use LSP's implementation of the Jones scattering model,²⁹ which assumes a scattering "field" calculated from the average velocity and temperature of species (assumed to be Maxwellian), avoiding the need to calculate individual collisions between particles. Particle velocities are then modified by this field according to a collision rate. Most PIC codes which include collision models use the Spitzer collision rate,³⁰ which considers collisions in an ideal plasma

$$\nu_{ei} = 4\sqrt{2\pi} \frac{Z^2}{3\sqrt{m_e}} \left(\frac{e^2}{4\pi\epsilon_0} \right)^2 \frac{n_i \ln \Lambda_c}{T_e^{3/2}}, \quad (4)$$

where n_i is the ion density, T_e is the electron temperature, and $\ln \Lambda_c$ is the Coulomb logarithm—in LSP, this is calculated as $\ln \Lambda_c = 23 - \ln((n_e/\text{cm}^3)^{1/2} Z (T_e/\text{eV})^{-3/2})$,³¹ with a minimum value of 2.

This is valid in the case of a hot, dilute plasma, where there are many particles in the Debye sphere. In the conditions needed to model the transition from neutral atoms to ionization in 8CB, electron densities up to $n_e = 3.3 \times 10^{23}/\text{cm}^3$ must be represented, but at a temperature initially < 10 eV to avoid ionization before the laser arrives. Temperatures under 225 eV at this density result in fewer than 10 electrons per Debye sphere, while temperatures under ~ 1000 eV have fewer than 100 particles. In the low temperature limit, the Spitzer rate is inaccurate and continues to increase as temperature drops. The simplest way to avoid this is by capping the collision rate ν_{ei} at some value ν_{max} coarsely mimicking the saturation of the rate that actually takes place. Above a transition temperature T_0 , LSP's standard Spitzer model is used, and below T_0 the collision frequency is held constant at ν_{max}

$$\nu_{ei}[T_e] = \begin{cases} \nu_{Spitzer}[T_e] & T_e > T_0, \\ \nu_{max} & T_e \leq T_0. \end{cases} \quad (5)$$

In this work, different values of ν_{max} were tested for their effects on low-intensity reflectance. As Fig. 1 shows, below a laser intensity of 10^{14} W/cm² the reflectance was nearly constant for a given ν_{max} with only limited effect on the reflectance behavior above 10^{15} W/cm². For this work, $\nu_{max} = 5 \times 10^{15}$ Hz, corresponding to $T_0 \simeq 170$ eV, or roughly 7 electrons per Debye sphere. This is well resolved by the time step chosen for the simulation but acts mainly as a tuning parameter here, chosen in concert with the MPI coefficient to give the best match to experiment. Two physically motivated possibilities for ν_{max} are

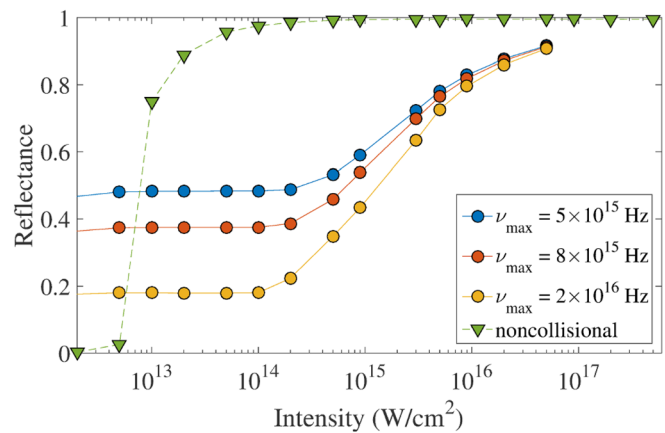


FIG. 1. Effect of varying collision rate cap ν_{max} on reflectance as a function of intensity. Circles are 2D simulations using multiphoton ionization at the indicated intensity; and lines are added to guide the eye. For blue, orange, and yellow circles, in the low field limit ($I < 10^{15}$ W/cm²), the reflectance is constant for a given ν_{max} and increases as ν_{max} decreases. At higher intensities, the difference as a function of ν_{max} becomes negligible. In the absence of collisions (green triangles), reflectance rapidly approaches 1 as intensity is increased over the ionization threshold, and no absorptive losses occur.

discussed below and will be investigated in future work. These collision frequencies are shown in Fig. 2 as a function of T_e : the unmodified Spitzer rate is shown in blue, the value used in this work is shown in orange, and the maximum frequency resolvable by these simulations is plotted as a dashed line.

When Debye shielding is no longer a valid model, a more useful scale length is the interparticle spacing. This can be used as a surrogate for the average mean free path between particle collisions—for electron-ion collisions, this is $\lambda_{mfp} \sim (n_i)^{-1/3}$. The average time an electron takes to travel λ_{mfp} is $\tau_{mfp} = \lambda_{mfp}/v_{th}$, where the electron thermal velocity is $v_{th} = \sqrt{3k_B T_e/m_e}$ and k_B is the Boltzmann constant. Using this approximation, $\nu_{max} = 1/\tau_{mfp}$, which is $\sim 2.8 \times 10^{15}$ Hz for a liquid crystal plasma mirror temperature and density of $n_i = 5.5 \times 10^{22}/\text{cm}^3$, so that $T_0 \sim 320$ eV (purple line).

As the plasma temperature goes to 0, degeneracy determines the characteristic (Fermi) energy of the electrons $E_F = \hbar^2/(2m_e)(3\pi^2 n_e)^{2/3}$. Setting $T_0/(m_e c^2) \sim E_F$ yields a much higher collision rate cap—this is the approach used by Sentoku and Kemp.³² In this model, $T_0 \sim 17$ eV for $n_e = 3.3 \times 10^{23}/\text{cm}^3$, with $\nu_{max} = 1.6 \times 10^{17}$ Hz (green), which would require a much smaller simulation time step.

V. LOW FIELD BEHAVIOR

The low field reflectance of a plasma mirror is vital to model correctly as otherwise the degree of transmission of the laser's leading edge will not be captured. LSP incorporates a spatially varying dielectric model which was used to overlay the plasma mirror region with $n = 1.53$ to properly model the thin film reflection characteristics before the neutral atoms are ionized. Figure 3(a) shows this model interacting with the laser electric field at the time the peak of the pulse

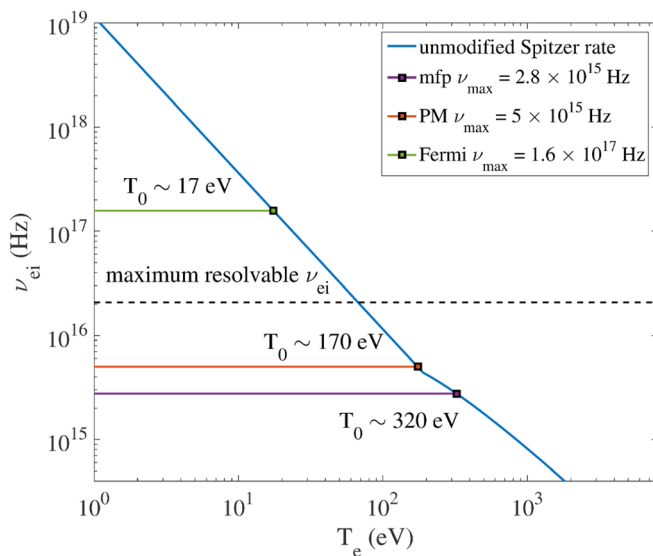


FIG. 2. Spitzer collision rate (blue) as a function of plasma temperature T_e . Two parameters can be adjusted to account for unphysical low-temperature behavior: cutoff temperature and maximum collision rate frequency. Mean free path based ν_{max} (purple), Fermi energy based ν_{max} (green), and $\nu_{max} = 5 \times 10^{15}$ Hz (orange), the value used for these simulations as described in the text. Frequencies above the dashed line cannot be resolved by the simulation time step used here.

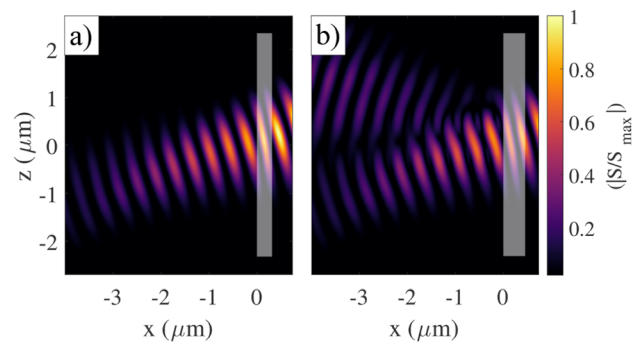


FIG. 3. (a) The simulation plasma mirror thickness is tuned for Fresnel antireflection (270 nm here) in the low-field limit for the index of refraction of the chosen material (here the liquid crystal 8CB) using the LSP's dielectric model. The Poynting vector magnitude at the time of the peak of the pulse is plotted as the laser refracts in the target (white shaded rectangle). (b) The Poynting vector magnitude is plotted at the same point in time with a plasma mirror thickness chosen to maximize low-field reflectance (400 nm). A substantial amount of the laser pulse is reflected.

reaches the target location which is here devoid of atoms to ionize. The target thickness is at a reflectance minimum for this laser wavelength, angle of incidence, and index of refraction, and as a result the light is predominantly transmitted. By contrast Fig. 3(b) shows the same point in time but now with the target thickness appropriate for maximum reflection. The amount of reflected light was determined by measuring the field flux normal to the laser outlet boundary. For a target thickness of 270 nm, the low-field reflectance in the simulation was observed to be 0.2%, in agreement with experiment.

VI. SIMULATION DIMENSIONALITY

2D3V simulations allowed the rapid survey of different numerical options over a wide range of laser intensities. While 2D simulations can provide valuable qualitative insight into many cases, they often fall short when quantitative agreement is desired.

Here, the intensity falloff of the laser beam in the simulation's virtual dimension (the dimension normal to the 2D grid) is neglected in 2D simulations, as is the corresponding drop in reflectance. To correct for this effect, a 3D approximation was achieved by treating each 2D simulation as a slice of the 3D pulse profile [Figs. 4(a) and 4(b)], and many such runs were summed over, weighted by their fractional contribution to the total pulse energy. This took into account the shape of the laser focus in both transverse directions, integrating numerically out to $2.7\omega_0$ in the virtual dimension to match the width of the 2D simulations. The equation used to find the 3D reflectance was

$$R_{3D} = \frac{\sum_n R_{2D,n} \int_{y_{n-1}}^{y_n} I(y) dy}{\sum (I(y))}, \quad (6)$$

for the 2D simulation reflectivities $R_{2D,n}$ and spatial intensity distributions $I(y)$. The y dimension of the beam, taken from $-2.7\omega_0$ to $2.7\omega_0$, is divided into slices based on the number of simulations. For example, results from 25 2D simulations are plotted in Fig. 4(c) at or below 2×10^{16} W/cm², so for this intensity $y_n = 5\omega_0/24 \times n$ for $n = 0$ to 24. To demonstrate the size of this correction, a series of 2D simulations were performed at a range of intensities, as well as two fully 3D

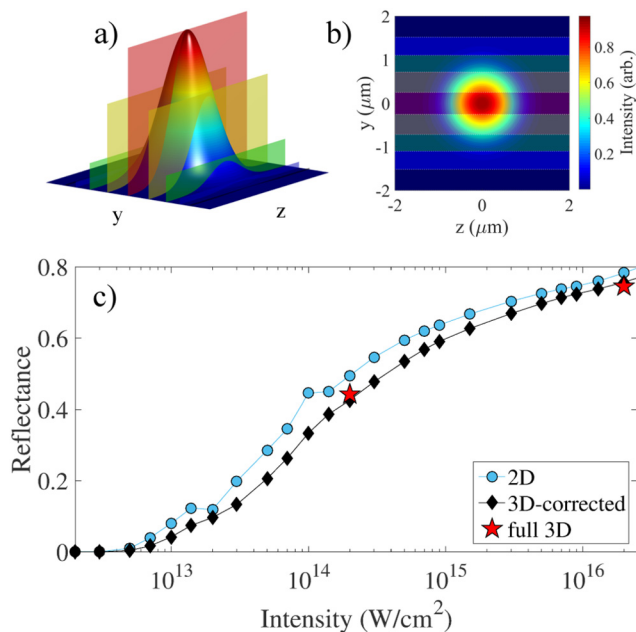


FIG. 4. Representation of the correction method for simulation dimensionality. (a) An intensity distribution with y and z dependence is not well approximated by any one 2D line beam (colored slices). (b) Top-down view of intensity distribution, showing the individual 2D3V simulation slices which contribute to the full beam schematically. In this depiction, x is the propagation direction of the laser and y is the simulation virtual dimension. (c) Comparison between uncorrected 2D simulated reflectance (light blue dashed line) and 3D-corrected results (black diamonds) using the method described in Sec. VI. Full 3D simulations were conducted at 2×10^{14} and 2×10^{16} W/cm² (red stars), which agree well with 3D-corrected results. All simulations in this plot were done with a 20 fs Gaussian pulse to ease computational constraints in the 3D case and used an MPI coefficient $C = 1 \times 10^{-9}$ kV/cm and collision frequency $\nu_{\max} = 5 \times 10^{15}$ Hz.

simulations at 2×10^{14} and 2×10^{16} W/cm². In all of these, a 20 fs Gaussian pulse was used to reduce the computation costs of the 3D simulations. Figure 4(c) shows the reflectances obtained from these 3D simulations (red stars) and how they compare to the uncorrected 2D (light blue circles) and 3D-corrected 2D results (black diamonds). Importantly, the 3D-corrected 2D results, encompassing more than 20 simulations, are achieved at less than 10% the computational cost of a single full 3D simulation. At 2×10^{16} W/cm², the error with respect to the 3D result is reduced from 5% to 2% by performing a 3D correction, and at 2×10^{14} W/cm² this improves, with an error of 12% reduced to 4%. The error in uncorrected 2D simulations is generally larger at lower intensities, which indicates that this method is necessary in order to examine effects dependent on ionization threshold, such as pulse shortening.

This technique can be extended to consider the reflected mode of the laser. In Fig. 5, the time-integrated laser flux has been plotted at $x = -0.5 \mu\text{m}$ from the plasma mirror front surface for 2×10^{16} W/cm². In Fig. 5(a), this is done using integrated fluxes from 2D simulations, stacked according to the method described above; in Fig. 5(b), a moving average is applied over 20 points (60 nm) in z . In Fig. 5(c), a lineout from each of these images is plotted along $z = 0$ to better show their agreement. Comparing these results to the mode obtained from the full

3D simulation in Fig. 5(d), it can be seen that although some fine structure in the center of the 3D simulation's beam is not captured in the 2D simulations, good agreement is obtained overall both in the 2D simulation dimension (z) and the virtual dimension (y). This suggests that at least in some cases, 2D simulations can also be used to evaluate plasma mirror reflected beam quality and other parameters without the need for 3D simulations.

VII. RESULTS AND DISCUSSION

Figure 6 shows the experimental s-polarization data along with two simulation curves using different models. Using an MPI ionization model with a Gaussian pulse shape with $C = 1 \times 10^{-9}$ cm/kV and collisions with $\nu_{\max} = 5 \times 10^{15}$ Hz results in an excellent match to experiment (green diamonds vs red triangles) over three orders of magnitude in intensity. Simulations with the same MPI coefficient and ν_{\max} , but using a sech^2 pulse (blue diamonds), show very similar results, indicating that pulse shape does not have a strong effect on the integrated reflectance (the throughput) of the plasma mirror. Since the peak intensities used were the same between the different pulse shapes, the sech^2 pulse contained 1.06 times the energy in the Gaussian pulse.

The rapid decrease in reflectance beginning at 5×10^{16} W/cm² is an interesting feature and is not captured by simulations. Similar trends as a function of laser intensity have been observed in other experiments measuring energy absorption.^{9,33} In some experiments, the rollover intensity is $\sim 10^{18}$ W/cm², where relativistic effects become important at the wavelengths used, but the reflectance drop occurs at about an order of magnitude too low with liquid crystal plasma mirrors and most other materials for this to contribute. Laser contrast is a natural suspect when performance degrades as intensity is increased, but it can be discounted at these intensities for the laser used to obtain the experimental data¹⁷ used as a benchmark here. In order for a prepulse to drive plasma mirror degradation beginning at 5×10^{16} W/cm², the laser contrast would need to be 5×10^{-4} or worse, and this system³⁴ has contrast in excess of 10^{-5} at times > 1 ps before the main pulse.

A few nonrelativistic mechanisms could be responsible for this reflectance rollover. Inverse bremsstrahlung (IB) absorption, where an electron absorbs a photon during a collision with an ion, can take place in preplasma up to the critical density and has been shown³⁵ to have an absorption coefficient $\eta_{IB} = 1 - \exp(-32/15 \nu_{ei}(n_{cr} L_n/c))$, where L_n is the preplasma scale length and n_{cr} is the critical density. η_{IB} is large for laser intensities up to 10^{17} W/cm², for low temperature plasmas, and for large L_n .³⁶ Another potential contributing mechanism is sheath-transit absorption (STA),³⁷ more commonly known by its two limiting cases—sheath inverse bremsstrahlung (SIB)³⁸ and the anomalous skin effect (ASE).³⁹ When $\nu_{th}/\nu_{ei} > \delta_s$, the plasma skin depth, electrons can travel out of the skin depth, carrying laser energy away into the plasma bulk. STA is an important process for steep plasma gradients.⁴⁰ It is difficult to be certain which of these mechanisms is more likely to have been responsible since preplasma was not measured in the liquid crystal plasma mirror experiment, but it seems probable that the L_n was small—the laser was defocused for this experiment, and any prepulses likely transmitted through the target without ionizing.

For either STA or IB, recent work⁴¹ suggests a source of the discrepancy between these simulations and experiment above the typical plasma mirror operating intensities. In that work, it was shown to be

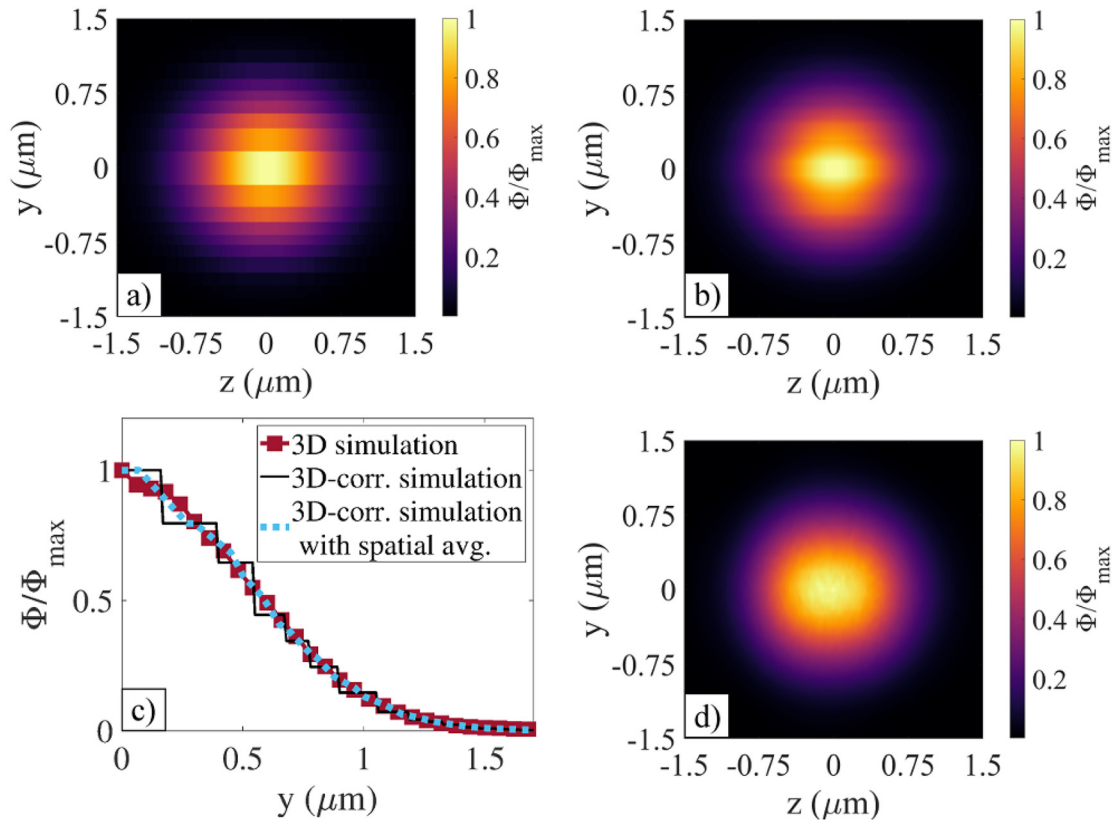


FIG. 5. (a) 2D simulations reconstructed to show reflected time-integrated flux perpendicular to propagation for $I = 2 \times 10^{16} \text{ W/cm}^2$. (b) Result from (a) with a 20 point (60 nm) moving average in z applied. (c) Lineout along $z = 0$ from parts (a), (b), and (d). 3D simulations (red squares) are fairly well matched by reconstruction from 2D simulations with and without spatial averaging (blue circles, black lines), with the largest discrepancy near peak intensity. (d) 3D simulated time-integrated flux perpendicular to propagation for $I = 2 \times 10^{16} \text{ W/cm}^2$.

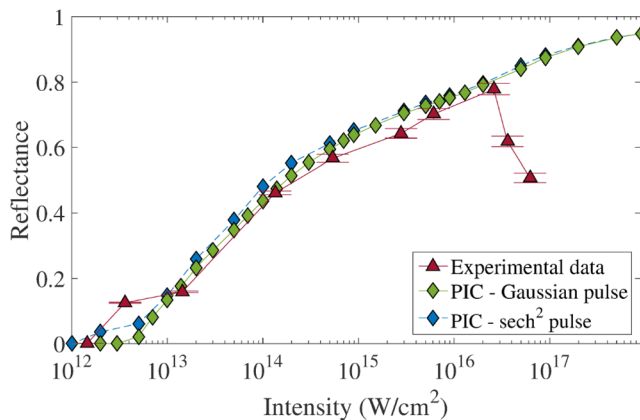


FIG. 6. Laser reflectance for s-polarization obtained from LSP PIC simulations (green diamonds). The experimental results¹⁷ (red triangles) are shown for comparison. Use of a sech^2 pulse with 60 fs FWHM shows a similar behavior (blue diamonds). Intensities corresponding to a Keldysh parameter $\gamma < 0.5$ for H^+ and C^{1+} require the use of a multiphoton ionization model. All simulation results are 3D-corrected with $\nu_{\max} = 5 \times 10^{15} \text{ Hz}$; the MPI ionization coefficient used is $1 \times 10^{-9} \text{ cm/kV}$.

necessary to resolve δ_s with 5–50 cells per skin depth in order to capture how laser energy is transmitted from the skin depth into the bulk of the target, where $\delta_s/\Delta x = 3.7$ for these simulations. Another potential source of error is under-resolving the Debye length. During one of these simulations, the density can reach several hundred times critical density and temperatures as high as 100 eV. Although the simulation was numerically stable to Debye heating effects, absorption processes may require that this length is resolved. Pinpointing the appropriate simulation parameters to model this high intensity behavior will be a part of future work focusing on physics outside of the plasma mirror operation discussed here.

The sensitivity of these results was tested by slightly varying the multiphoton ionization coefficient used, shown in Fig. 7. Compared to $C = 1 \times 10^{-9} \text{ cm/kV}$ (blue diamonds), $C = 8 \times 10^{-10} \text{ cm/kV}$ (orange diamonds) yields a much higher onset intensity for plasma mirror operation ($5 \times 10^{13} \text{ W/cm}^2$), similar to what was observed when using ADK ionization (green squares). Additionally, the reflectance simulated with this ionization coefficient falls dramatically above 10^{15} W/cm^2 , and at no point do the results for this value agree well with experiment. When C is raised to $2 \times 10^{-9} \text{ cm/kV}$ (yellow diamonds), the ionization threshold is only slightly affected. This ionization coefficient produces reflectances that are in reasonable agreement with

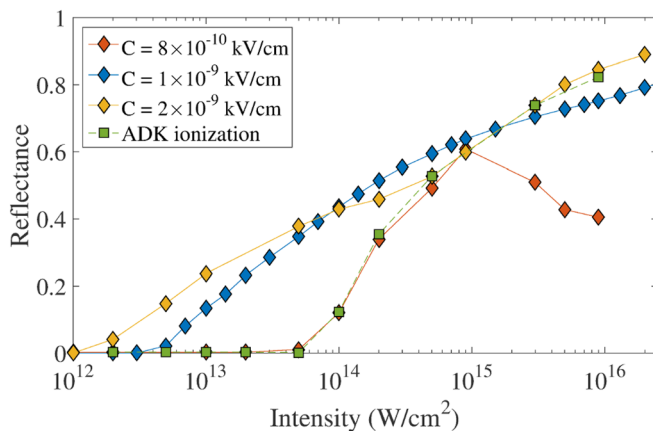


FIG. 7. Laser reflectance for s-polarized light obtained from LSP PIC simulations plotted as a function of incident laser intensity for different MPI ionization coefficients. The best fit to experimental data, $C = 1 \times 10^{-9}$ cm/kV (blue diamonds). Lowering C to 8×10^{-10} cm/kV (orange diamonds) raises the ionization threshold to $\sim 5 \times 10^{13}$ W/cm² with a drop in reflectance above 10^{15} W/cm². Raising C to 2×10^{-9} cm/kV (yellow diamonds) not only causes the plasma mirror to initiate at too low an intensity, as expected, but also produces a fundamentally different curve as a function of intensity, as opposed to a simple shift. Ionization using ADK (green squares) is shown for comparison. Connecting lines are added to guide the eye.

experimental data at each intensity, but when taken together, they do not capture the overall shape for reflectance as a function of intensity, showing that adjusting this value does not simply produce scaled or shifted results, but directly affects the underlying physics.

VIII. CONCLUSION

Over the orders of magnitude responsible for this plasma mirror's operation (2×10^{12} – 2×10^{16} W/cm²), the presented quantitative agreement between simulation and experiment is excellent. Using a multiphoton ionization model and incorporating low-temperature modifications to the collision model, this framework can now be used to make predictions about changes to reflected pulse shape and beam profile. Furthermore, if enough is known about reflectance as a function of intensity, this approach could in principle be adapted to any pulse-cleaning plasma mirror material. Finally, the 3D reconstruction technique demonstrated here will be an important tool not only for increased efficiency when studying intense lasers interacting with other dielectrics but also for investigating aspects that require large simulation spaces and time scales such as the impact on reflected mode due to surface morphology evolution.

ACKNOWLEDGMENTS

We thank S. C. Wilks and A. J. Kemp for useful discussions. This work was performed under the auspices of the U.S. Department of Energy by Lawrence Livermore National Laboratory under Contract No. DE-AC52-07NA27344 and was supported by DOE Office of Science, Fusion Energy Sciences under Contract No. DE-FOA-0001664, the NNSA under Contract No. DE-FC52-0003107, and by an allocation of computing time from the Ohio Supercomputer Center.

This document was prepared as an account of work sponsored by an agency of the United States government. Neither the United

States government nor Lawrence Livermore National Security, LLC, nor any of their employees makes any warranty, expressed or implied, or assumes any legal liability or responsibility for the accuracy, completeness, or usefulness of any information, apparatus, product, or process disclosed, or represents that its use would not infringe privately owned rights. Reference herein to any specific commercial product, process, or service by trade name, trademark, manufacturer, or otherwise does not necessarily constitute or imply its endorsement, recommendation, or favoring by the United States government or Lawrence Livermore National Security, LLC. The views and opinions of authors expressed herein do not necessarily state or reflect those of the United States government or Lawrence Livermore National Security, LLC, and shall not be used for advertising or product endorsement purposes.

REFERENCES

- ¹P. McKenna, D. Carroll, O. Lundh, F. Nürnberg, K. Markey, S. Bandyopadhyay, D. Batani, R. Evans, R. Jafer, S. Kar *et al.*, *Laser Part. Beams* **26**, 591–596 (2008).
- ²D. Batani, R. Jafer, M. Veltcheva, R. Dezulian, O. Lundh, F. Lindau, A. Persson, K. Osvay, C.-G. Wahlström, D. C. Carroll, P. McKenna, A. Flacco, and V. Malka, *New J. Phys.* **12**, 045018 (2010).
- ³C. M. Brenner, A. P. L. Robinson, K. Markey, R. H. H. Scott, R. J. Gray, M. Rosinski, O. Deppert, J. Badziak, D. Batani, J. R. Davies, S. M. Hassan, K. L. Lancaster, K. Li, I. O. Musgrave, P. A. Norreys, J. Pasley, M. Roth, H.-P. Schlenvoigt, C. Spindloe, M. Tatarakis, T. Winstone, J. Wolowski, D. Wyatt, P. McKenna, and D. Neely, *Appl. Phys. Lett.* **104**, 081123 (2014).
- ⁴D. von der Linde, T. Engers, G. Jenke, P. Agostini, G. Grillon, E. Nibbering, A. Mysyrowicz, and A. Antonetti, *Phys. Rev. A* **52**, R25 (1995).
- ⁵M. Schollmeier, A. B. Sefkow, M. Geissel, A. V. Arefiev, K. A. Flippo, S. A. Gaillard, R. P. Johnson, M. W. Kimmel, D. T. Offermann, P. K. Rambo, J. Schwarz, and T. Shimada, *Phys. Plasmas* **22**, 043116 (2015).
- ⁶F. Wagner, S. Bedacht, A. Ortner, M. Roth, A. Tauschwitz, B. Zielbauer, and V. Bagnoud, *Opt. Express* **22**, 29505 (2014).
- ⁷G. Doumy, F. Quéré, O. Gobert, M. Perdrux, P. Martin, P. Audebert, J. C. Gauthier, J.-P. Geindre, and T. Wittmann, *Phys. Rev. E* **69**, 026402 (2004).
- ⁸B. Dromey, S. Kar, M. Zepf, and P. Foster, *Rev. Sci. Instrum.* **75**, 645 (2004).
- ⁹C. Ziener, P. Foster, E. Divall, C. J. Hooker, M. Hutchinson, A. J. Langley, and D. Neely, *J. Appl. Phys.* **93**, 768 (2003).
- ¹⁰L. Obst, J. Metzkes-Ng, S. Bock, G. E. Cochran, T. E. Cowan, T. Oksenhendler, P. L. Poole, I. Prencipe, M. Rehwald, C. Rödel, H.-P. Schlenvoigt, U. Schramm, D. W. Schumacher, T. Ziegler, and K. Zeil, *Plasma Phys. Controlled Fusion* **60**, 054007 (2018).
- ¹¹A. Pukhov, T. Baeva, D. a d Brüggé, and S. Münster, *Eur. Phys. J. D* **55**, 407 (2009).
- ¹²C. Thauray, F. Quéré, J.-P. Geindre, A. Levy, T. Ceccotti, P. Monot, M. Bougeard, F. Réau, P. d'Oliveira, P. Audebert, R. Marjoribanks, and P. Martin, *Nat. Phys.* **3**, 424 (2007).
- ¹³N. M. Naumova, C. P. Hauri, J. A. Nees, I. V. Sokolov, R. Lopez-Martens, and G. A. Mourou, *New J. Phys.* **10**, 025022 (2008).
- ¹⁴G. G. Scott, V. Bagnoud, C. Brabetz, R. J. Clarke, J. S. Green, R. I. Heathcote, H. W. Powell, B. Zielbauer, T. D. Arber, P. McKenna, and D. Neely, *New J. Phys.* **17**, 033027 (2015).
- ¹⁵S. K. Mishra, A. Andreev, and M. P. Kalashnikov, *Opt. Express* **25**, 11637 (2017).
- ¹⁶A. Lawrence-Douglas, "Ionisation effects for laser-plasma interactions by particle-in-cell code," Ph.D. thesis (University of Warwick, 2013).
- ¹⁷P. L. Poole, A. Krygier, G. E. Cochran, P. S. Foster, G. G. Scott, L. A. Wilson, J. Bailey, N. Bourgeois, C. Hernandez-Gomez, D. Neely, P. P. Rajeev, and D. W. Schumacher, *Sci. Rep.* **6**, 32041 (2016).
- ¹⁸D. Welch, D. Rose, R. Clark, T. Genoni, and T. Hughes, in *Proceedings of the 18th International Conference on the Numerical Simulation of Plasmas* (2004), Vol. 164, p. 183.

- ¹⁹P. L. Poole, C. D. Andereck, D. W. Schumacher, R. L. Daskalova, S. Feister, K. M. George, C. Willis, K. U. Akli, and E. A. Chowdhury, *Phys. Plasmas* **21**, 063109 (2014).
- ²⁰P. L. Poole, C. Willis, G. E. Cochran, R. T. Hanna, C. D. Andereck, and D. W. Schumacher, *Appl. Phys. Lett.* **109**, 151109 (2016).
- ²¹P. B. Corkum, *Phys. Rev. Lett.* **71**, 1994 (1993).
- ²²L. Keldysh, *J. Exp. Theor. Phys.* **20.5**, 1307 (1965).
- ²³M. Ammosov, *J. Exp. Theor. Phys.* **64**, 1191 (1986).
- ²⁴N. B. Delone and V. P. Krainov, *Phys.-Usp.* **41**, 469 (1998).
- ²⁵F. A. Ilkov, J. E. Decker, and S. L. Chin, *J. Phys. B: At., Mol. Opt. Phys.* **25**, 4005 (1992).
- ²⁶J. Sansonetti and W. Martin, *J. Phys. Chem. Ref. Data* **34**, 1559 (2005).
- ²⁷S. Lias, "Ionization energy evaluation," in *NIST Chemistry WebBook, NIST Standard Reference Database Number 69* (National Institute of Standards and Technology, Gaithersburg, 2018).
- ²⁸C. J. G. J. Uiterwaal, D. Xenakis, D. Charalambidis, P. Maragakis, H. Schröder, and P. Lambropoulos, *Phys. Rev. A* **57**, 392 (1998).
- ²⁹M. E. Jones, D. S. Lemons, R. J. Mason, V. A. Thomas, and D. Winske, *J. Comput. Phys.* **123**, 169 (1996).
- ³⁰L. Spitzer, *Physics of Fully Ionized Gases* (Courier Corporation, 1963).
- ³¹J. D. Huba, *Plasma Physics* (Naval Research Laboratory, Washington, DC, 2018), pp. 1–71.
- ³²Y. Sentoku and A. J. Kemp, *J. Comput. Phys.* **227**, 6846 (2008).
- ³³Y. Ping, R. Shepherd, B. F. Lasinski, M. Tabak, H. Chen, H. K. Chung, K. B. Fournier, S. B. Hansen, A. Kemp, D. A. Liedahl, K. Widmann, S. C. Wilks, W. Rozmus, and M. Sherlock, *Phys. Rev. Lett.* **100**, 085004 (2008).
- ³⁴Y. Tang, C. J. Hooker, O. V. Chekhlov, S. Hawkes, B. Parry, K. Ertel, J. Collier, and P. P. Rajeev, in *CLEO: 2013* (Optical Society of America, 2013), p. CTu2D.4.
- ³⁵V. Ginsburg, *Propagation of Electromagnetic Waves in Plasmas* (Gordon and Breach, New York, 1960).
- ³⁶S. C. Wilks and W. L. Kruer, *IEEE J. Quantum Electron.* **33**, 1954 (1997).
- ³⁷T. B. Yang, W. L. Kruer, A. B. Langdon, and T. W. Johnston, *Phys. Plasmas* **3**, 2702 (1996).
- ³⁸P. J. Catto and R. M. More, *Phys. Fluids* **20**, 704 (1977).
- ³⁹E. S. Weibel, *Phys. Fluids* **10**, 741 (1967).
- ⁴⁰P. Gibbon, *Short Pulse Laser Interactions with Matter: An Introduction* (Imperial College Press, 2005).
- ⁴¹A. J. Kemp and L. Divol, *Phys. Plasmas* **23**, 090703 (2016).